Journal of Wuhan University of Technology-Mater. Sci. Ed. www.jwutms.net Oct. 2018

1205

Effect of Cl⁻ Concentration on the Corrosion Behavior of 16Mn Steel in Saturated H₂S/CO₂ Solution

SONG Wenming[1,2], YANG Guirong[1]*, LIAO Bingbing[1], LI Jian [3], MA Ying[1], HAO Yuan[1]

(1. State Key Laboratory of Advanced Processing and Recycling of Nonferrous Metals, Lanzhou University of Technology, Lanzhou 730050, China; 2. Lanzhou Petroleum Machinery Institute, Lanzhou 730000, China; 3. Wuhan Research Institute of Materials Protection, Wuhan 430030, China)

Abstract: The corrosion behavior of 16Mn steel was studied in saturated H_2S or H_2S/CO_2 solutions containing different Cl^- concentrations at 80 ℃. The microstructure and chemical composition of the corrosion products were investigated through scanning electron microscopy, energy-dispersive X-ray spectroscopy, EPMA, and X-ray diffraction. Results showed that the corrosion rate decreased with increasing Cl^- concentration in saturated H_2S or H_2S/CO_2 solution at pH 4. Conversely, the corrosion rate increased with increasing Cl^- concentration in saturated H_2S solution at pH 6. The relative H^+ concentration decreased because of the increase of Cl^- concentration at pH 4, and Cl^- acted as a catalyst in the corrosive medium at pH 6 because the net H^+ concentration decreased obviously compared with the condition at pH4. Cl^- promoted the formation of Fe-deficient iron sulfide at pH 4, and the opposite effect was observed in the nearly neutral solution. The corrosion rate increased firstly with increasing Cl^- concentration and then decreased in the saturated H_2S/CO_2 solution at pH 6. The corrosion products were mainly composed of two kinds of iron sulfide. Sulfide FeS_{1-x} was a kind of tetragonal crystal, whereas the other was the hexagonal/monoclinic iron sulfide $Fe_{1-x}S$. The corrosion film that was mainly composed of FeS_{1-x} did not confer a protective effect on the base metal. The atomic ratio of Fe/S was more than 1 for FeS_{1-x}. The appearance of sulfide FeS_{1-x} resembled a square block or small, needle-like, flocculent particles. The atomic ratio of Fe/S was less than 1 for $Fe_{1-x}S$, and the corrosion film mainly composed of $Fe_{1-x}S$ conferred some protective property on the base metal. The sulfide FeS_{1-x} exhibited a long claviform morphology with a hexagonal or quadrilateral cross-sectional shape.

Key words: 16Mn steel; acid corrosion; weight loss; microstructure; corrosion products

1   Introduction

Equipment and constructions in the oil and gas industry are a considerable part of all metal-based equipments worldwide. Safety and durability issues related to metal constructions and equipment are important concerns because corrosion failures can lead to costly repairs, plant shutdowns, health and environmental hazards under operating conditions. A problem in the production and transportation of sour oil and gas is the corrosion caused by the acid gases CO_2 and H_2S[1,2]. Along with the intensive

exploitation of oil and gas, the H_2S and CO_2 corrosion problem becomes much more severe as the water salinity, which involves different Cl^- concentration, the service temperature，the partial pressures of CO_2 and H_2S increases[1-4]. Prediction of service life and the maintenance period of the equipment in oil and gas production and transportation under the complicated corrosive conditions is a difficult task[5]. Corrosion-resistant alloys have long been available as a material selection option for the mitigation of CO_2 and H_2S corrosion. Even so, carbon steel is generally more cost-effective for use in constructing oil and gas facilities[6] and hence, is the most widely employed material for such purpose[6]. The internal corrosion of carbon steel pipelines in the presence of CO_2 and H_2S was first recognized in the 1940s and has been investigated for over 70 years[7].

Several studies have shown that the presence of H_2S could either accelerate or inhibit carbon steel corrosion depending on the partial pressure of H_2S. Earlier studies reported that at H_2S concentrations

1206

Vol.33 No.5 *SONG Wenming et al*: Effect of Cl⁻ Concentration on the Corrosion Behavior...

below 690 Pa, a protective iron sulfide film forms[8-10]. More recently, Ma *et al* claimed that H_2S provides a strong inhibition under special conditions of lower H_2S concentration ($\leqslant 0.04$ mmol dm^{-3}), pH of 3–5, and longer immersion time ($\geqslant 2$ h)[11]. Abelev *et al* also reported that 5 ppm H_2S exerts an inhibitory effect on corrosion in the presence of CO_2[12,13]. Sun systematically studied the kinetics of iron sulfide and iron carbonate scale formation in CO_2/H_2S corrosion using the weight-change method[14]. However, the model deviated considerably from their experimental data when the study was extended to conditions with H_2S partial pressures exceeding 10 bar. On the basis of the shortcoming of Sun's model, Hu *et al* reviewed the corrosion at a higher H_2S concentration and moderate temperature[15]. Depending on local practices, hydrogen permeation studies are performed with H_2S gas mixed with N_2[16,17] or with CO_2[18]. However, CO_2 is known to strongly affect corrosion. The cathodic reaction rate is known to be enhanced in aqueous solutions containing dissolved CO_2, compared with strong acid solutions at the same pH[19]. Besides this effect on the whole electrochemical kinetics and CO_2 might also directly influence the corrosive mechanism. Competitive adsorption among S^{2-}, HS^-, CO_3^{2-}, and other anions could modify the corrosive process[20]. However, no clear understanding has been achieved on the nature of the surface layer formed in CO_2/H_2S environments, especially in CO_2/H_2S environments with different Cl⁻ concentrations. Furthermore, only a few results have been reported on experiments conducted under saturated CO_2/H_2S solutions with different Cl⁻ concentrations.

Surface scale formation is an important factor governing corrosion rate[21]. Currently, how the variation in corrosive film composition affects corrosion rate remains unclear. A previous study suggested that the inhibiting or promoting effect is related to the formation of iron sulfide with different crystal structures, such as amorphous ferrous sulfide, mackinawite, cubic ferrous sulfide, pyrrhotite, troilite, and pyrite[22]. In this work, the corrosion behavior of commercial 16Mn steel was investigated in saturated H_2S or H_2S/CO_2 solution with different Cl⁻ concentrations at 80 ℃ and pH 4 and 6. Corrosion rates were determined through the weight-loss method. The appearance of corrosion products was observed through scanning electron microscopy (SEM). The composition of the corrosion products was analyzed through energy-dispersive X-ray spectroscopy (EDS) and X-ray diffraction (XRD). The corrosion

mechanism was also discussed.

2 Experimental

2.1 Sample preparation

The commercial 16Mn carbon steel adopted in this study was purchased with the following composition (wt%): 0.13%–0.19% C, 0.20%–0.60% Si, 1.20%–1.60% Mn, ≤0.30% Cr, ≤0.03% P, ≤0.03% S, ≤0.30% Ni, ≤0.25% Cu, and balanced Fe. The specimens were cut from the as-received 16Mn plates, and each specimen measured 50×25×2 mm^3. Next, the surfaces of all the specimens were mechanically ground using 120#, 300#, 500#, 800#, and 1000# emery papers in sequence. The specimen surfaces were washed with distilled water, ultrasonically cleaned with acetone for 3-5 min, and then washed once more using distilled water. All of the specimens were measured with a Vernier caliper, and then washed with acetone and distilled water using an ultrasonic cleaner. The prepared samples were stored in a vacuum desiccator prior to use.

2.2 Immersion tests

To compare the different corrosion behaviors of 16Mn in saturated H_2S and saturated CO_2/H_2S solutions with different Cl⁻ concentrations, solutions with different Cl⁻ concentrations (57, 100, and 170 ppm by mass) were prepared for use in all immersion experiments. Cl⁻ was derived from NaCl in the experimental solution. Two kinds of immersion solutions were adopted in this study: saturated H_2S solution and saturated CO_2/H_2S solution, each with different Cl⁻ concentrations. A steady flow of Ar_2 gas was continuously delivered into each solution containing a certain Cl⁻ concentration for 2 h to remove the oxygen dissolved in the solution. Then, the H_2S gas or gas mixture of H_2S/CO_2 was introduced into the solution until saturation. The pH of the solutions was adjusted to 4.0±0.1 or 6.0±0.1 before the coupon immersion and tuned once every 2 h. The pH was tested by using a pH tester and initially adjusted using 1 mol/L H_2SO_4 or 1 mol/L NaOH and then using acetic acid for finer adjustment. All experiments were conducted under stagnant conditions at a temperature of 80±0.1 ℃ in a thermostatic water bath. Five coupons were immersed in a 2 L testing solution in a closed vessel for each experimental condition. The H_2S gas or H_2S/CO_2 gas mixture was piped into the corrosive solution once every 2 h. All the coupons were removed from the corrosive solutions after 98 h. Two samples were washed with alcohol, dried, and afterward stored

in a vacuum desiccator for the analysis of corrosion appearance and chemical composition of corrosion products. The remaining samples were ultrasonically cleaned with acetone for 3-5 min to remove corrosion products, washed with alcohol, and weighed after drying. The corrosion rate under every condition was determined by the average value of the three samples' corrosion rate under the same condition. The corrosion rate was evaluated through mass loss calculated using the following equation:

$$R = \frac{8.76 \times 10^7 \times (M - M_1)}{STD}$$

where R is the corrosion rate, mm/a; M is the weight of the sample before corrosion testing, g; M_1 is the weight of the sample after corrosion testing, g; S is the total area of the sample, cm^2; T is the corrosion time, h; and D is the density of material, kg/m^3.

2.3 Corroded surface observation and corrosion product analysis

The surface morphology of the corroded specimens was examined using SEM and subjected to elemental analysis with EDS (JEOL-JSM-6700 field emission SEM–EDAX). The thickness of the corrosion film was observed through the cross-sectional micro-appearance, and the elemental distribution was analyzed through line scanning. XRD analysis was conducted using a Bruker D8 focus diffractometer employing Cu Kα radiation (λ=1.540 6 Å). The XRD patterns were used to identify the different phases present in the corrosion film formed on the steel surface in different kind corrosion solutions.

3 Results and discussion

3.1 Corrosion rate

Fig.1 shows the curves of corrosion rate of 16Mn steel at different Cl$^-$ concentrations in saturated H$_2$S and saturated H$_2$S/CO$_2$ solutions when the pH is 4 and 6, respectively. The corrosion rate decreases with increasing Cl$^-$ concentration in saturated H$_2$S solution at pH 4. The decreasing rate at the initial stage is higher than that when the Cl$^-$ concentration is more than 57 ppm. By contrast, the corrosion rate increases with increasing Cl$^-$ concentration in the saturated H$_2$S solution at pH 6; and the increasing rate at the initial stage is lower than that when the Cl$^-$ concentration exceeds 57 ppm. The corrosion rate in the saturated H$_2$S solution at pH 4 is higher than that in the saturated H$_2$S solution at pH 6 when the Cl$^-$ concentration is less than 110 ppm. Furthermore, the corrosion rate in the saturated H$_2$S solution at pH 4 is lower than that in the saturated H$_2$S solution at pH 6 when the Cl$^-$ concentration exceeds 110 ppm (Fig.1(a)). The corrosion rate of 16Mn steel decreases with increasing Cl$^-$ concentration in the saturated H$_2$S/CO$_2$ solution at pH 4, and the corrosion rate almost does not change when the Cl$^-$ concentration exceeds 100 ppm until 170 ppm. The corrosion rate reaches a maximum value at 0.29 mm/a at 100 ppm Cl$^-$ in the saturated H$_2$S/CO$_2$ solution at pH 6. The corrosion rate at 57 ppm Cl$^-$ nearly equals the corrosion rate at 170 ppm Cl$^-$ contained in the saturated H$_2$S/CO$_2$ solution at pH 6. The corrosion rate at pH 4 is always higher than that at pH 6 in the saturated H$_2$S/CO$_2$ solution (Fig.1(b)). The corrosion rate of 16Mn steel at pH 4 is normally higher than that at pH 6 in solution, which could be inferred from the above-mentioned corrosion situations in the two types of saturated solutions with different Cl$^-$ concentrations. Two main reasons can explain the above-mentioned results. First, the H$^+$ concentration in the corrosive solution at pH 4 is much higher than that at pH 6, which often results in an increase in the cathode reaction rate. The relative H$^+$ concentration
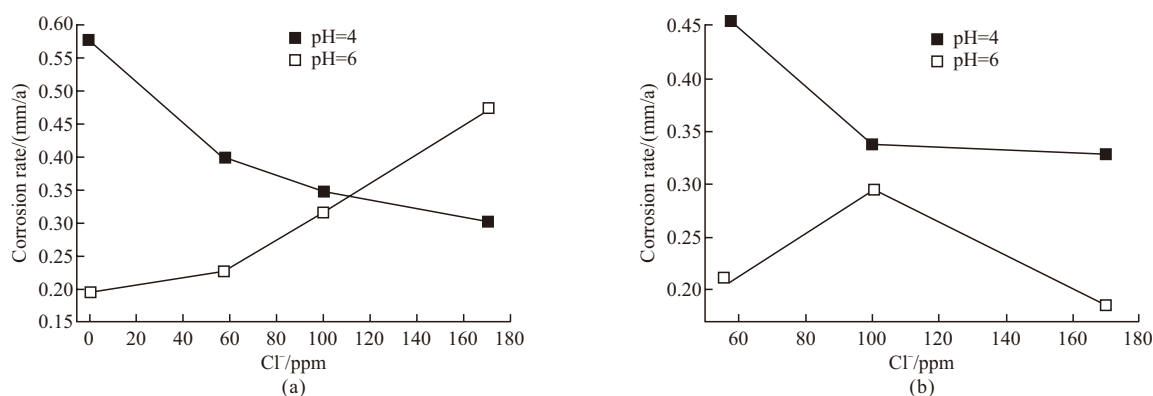

Fig.1 Corrosion rate of 16Mn steel in solutions with increasing Cl$^-$ concentration at T=80 ℃ and pH=4, 6: (a) Saturated H$_2$S solution and (b) saturated H$_2$S/CO$_2$ solution
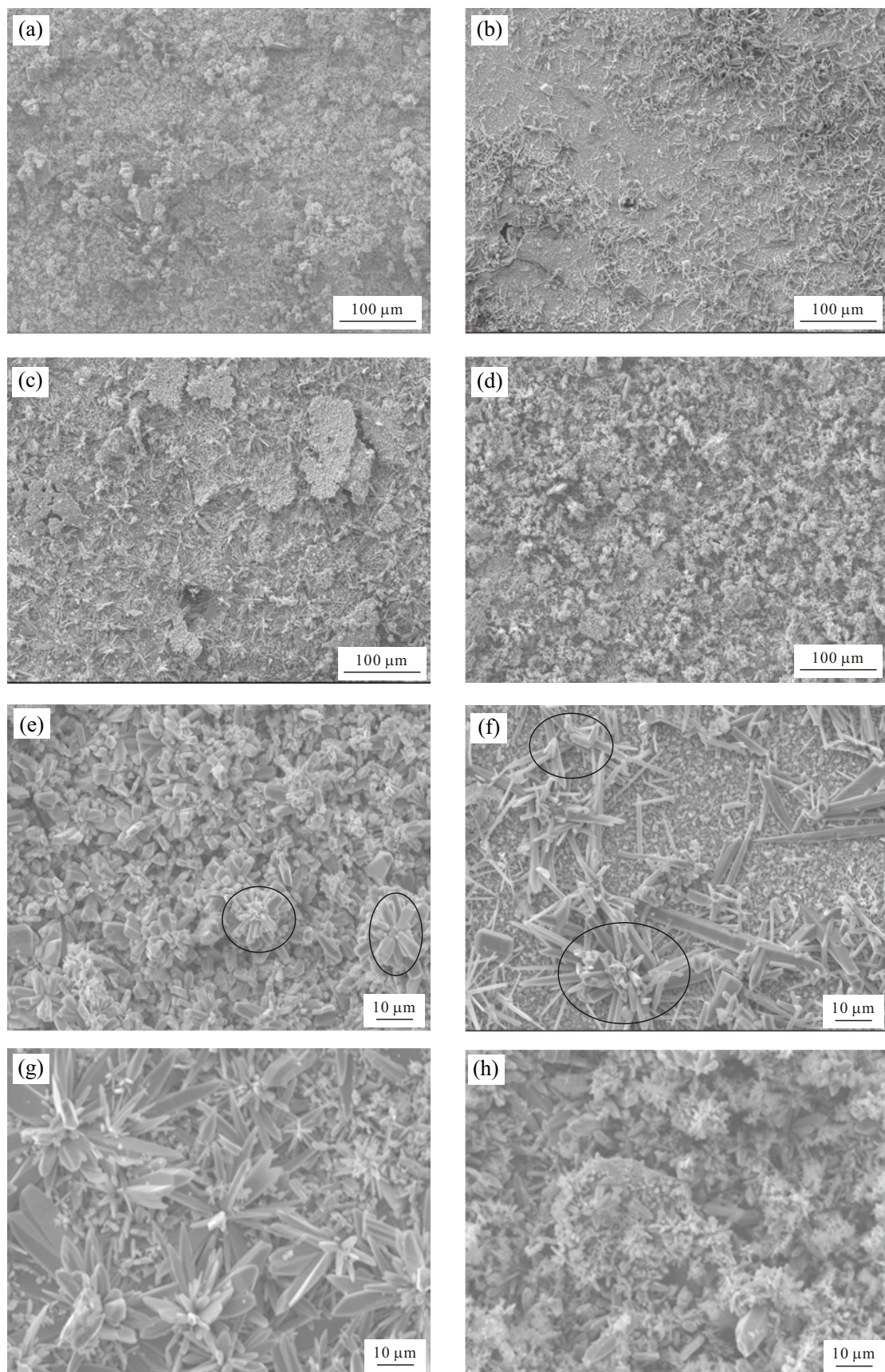
Fig.2 Corrosion morphologies of 16Mn steel in saturated H_2S solutions with different Cl⁻ concentrations at T=80 ℃ and pH=4, 6: (a) without Cl⁻, pH=4; (b) 170 ppm Cl⁻, pH=4; (c) without Cl⁻, pH=6; (d) 170 ppm Cl⁻, pH=6. (e)–(h) Magnified images of (a)-(d), respectively

decreases with increasing Cl^- concentration. Therefore, the corrosion rate decreases with increasing Cl^- concentration at pH 4. Second, the adsorption capacity of Cl^- at pH 4 is much stronger than that at pH 6 in solution, and the radius of Cl^- is smaller than the other anionic radii, resulting in the preferential adsorption of Cl^- to the metal surface. The quick adsorption of Cl^- would accelerate H^+ transmission during the corrosion process. Therefore, Cl^- becomes the corrosion catalyst and generally accelerates the corrosive process to a certain extent at pH 6[4].

3.2 Corrosion morphology

Fig.2 shows the corrosion morphology of 16Mn steel in saturated H_2S solution with different Cl^- concentrations at T=80 ℃ and different pH values. A corrosion film forms on every coupon surface (Figs.2(a)-(d)). The corrosion film in Fig.2(a) is the loosest, followed by those in Figs.2(d) and 2(b). The corrosion film in Fig.2(c) is the most compact among those in Fig.2. Figs.2(e)-2(h) display the magnified morphologies of those in Figs.2(a)-2(d), respectively. The external or cross-sectional shapes of the corrosion products at pH 4 and without Cl^- in solution mainly resemble square blocks (Fig.2(e)). The blocky corrosion products distribute irregularly, and parts of the corrosion products form clusters in Fig.2(e). The corrosion film composed of these corrosion products is loose, which corresponds to that in Fig.2(a). Many spherical clusters are present on the surface of the corrosion film shown in Fig.2(a), and the corrosion film presents layer surface characteristics of a honeycomb-like, porous membrane. Besides the irregular blocky corrosion products, a loose layer of tiny similar flocculent corrosion products are found on the surface of the corrosion film at 170 ppm Cl^- and pH 6 (Fig.2(h)). These tiny flocculent corrosion products present a cluster distribution, which corresponds to the relatively loose corrosion film shown in Fig.2(d). Acicular corrosion products are formed, with length-to-diameter ratios larger when the Cl^- concentration is 170 ppm at pH 4 than that in other conditions (Fig.2(f)). Moreover, the granular particles of the corrosion products of about 2 μm in diameter distribute densely underneath the acicular-shaped corrosion products. A small portion of the acicular corrosion products display a regular arrangement. The amount of acicular corrosion products increases at pH 6 and without Cl^- in solution (Fig.2(g)). The regular arrangement of the acicular corrosion products also becomes more obvious. Granular and long claviform corrosion products are found distributed irregularly on the surface of or in

between the acicular corrosion products. By comparing the shapes of the corrosion products and the compactness of the corrosion films between Figs.2(a) and 2(b), we notice that the compactness of the corrosion film increases with increasing Cl^- addition at pH 4. The change in compactness of the corrosion film contrasts with that at pH 6 (Figs.2(c) and 2(d)). A relatively dense corrosion film forms under this condition. The order of tightness of the corrosion films based on arrangement is as follows: regularly arranged>irregularly arranged>flocculent loose. Corrosion film tightness directly affects ion transport during the corrosion process. The resistance against anionic transport increases from the corrosive solution to the fresh surface of the 16Mn steel with increasing tightness of corrosion film. This increase in resistance then results in decreased corrosion rate. The tightness and morphology of the obtained corrosion films agree with the variation trend of the corrosion rate shown in Fig.1(a).

Fig.3 presents the corrosion morphology of 16Mn steel in saturated H_2S/CO_2 solutions with different Cl^- concentrations at T=80 ℃ and different pH values. A corrosion film is found on every coupon surface (Figs.3(a)-(d)), and Figs.3(e)-3(f) display the magnified morphologies of Figs.3(a)–3(d), respectively. The corrosion film surface presents loose cellular characteristics at pH 4 (Figs.3(a) and 3(b)), and the shape and arrangement of the corrosion products are irregular. The amount and tightness of the globular-clustered corrosion products in Fig.3(b) is greater than those in Fig.3(a). These findings are consistent with the corrosion rates that correspond to the corrosion conditions. The tightness of the corrosion film at pH 6 in Figs.3(c) and 3(d) is much higher than that in Figs.3(a) and 3(b) at pH 4. Many acicular corrosion products with different sizes are noticed on the surface of the corrosion film in Figs.3(c) and 3(d). The extent of orderly arrangement of the acicular corrosion products differs with varying Cl^- concentration. The shape of the corrosion products in acidic solution is characterized mainly as flocculent needles with some blocky corrosion products, and the loosely clustered corrosion film is composed of the needle-like, flocculent products shown in Figs.3(e) and 3(f). The corrosion products are composed of acicular or long, claviform and blocky corrosion products with regular arrangements, whereas the compact corrosion film consists of those shown in Figs.3(g) and 3(h). The corrosion rate of the sample covered with a compact and effective corrosion film is lower than that covered with a loose corrosion film. The globular-clustered
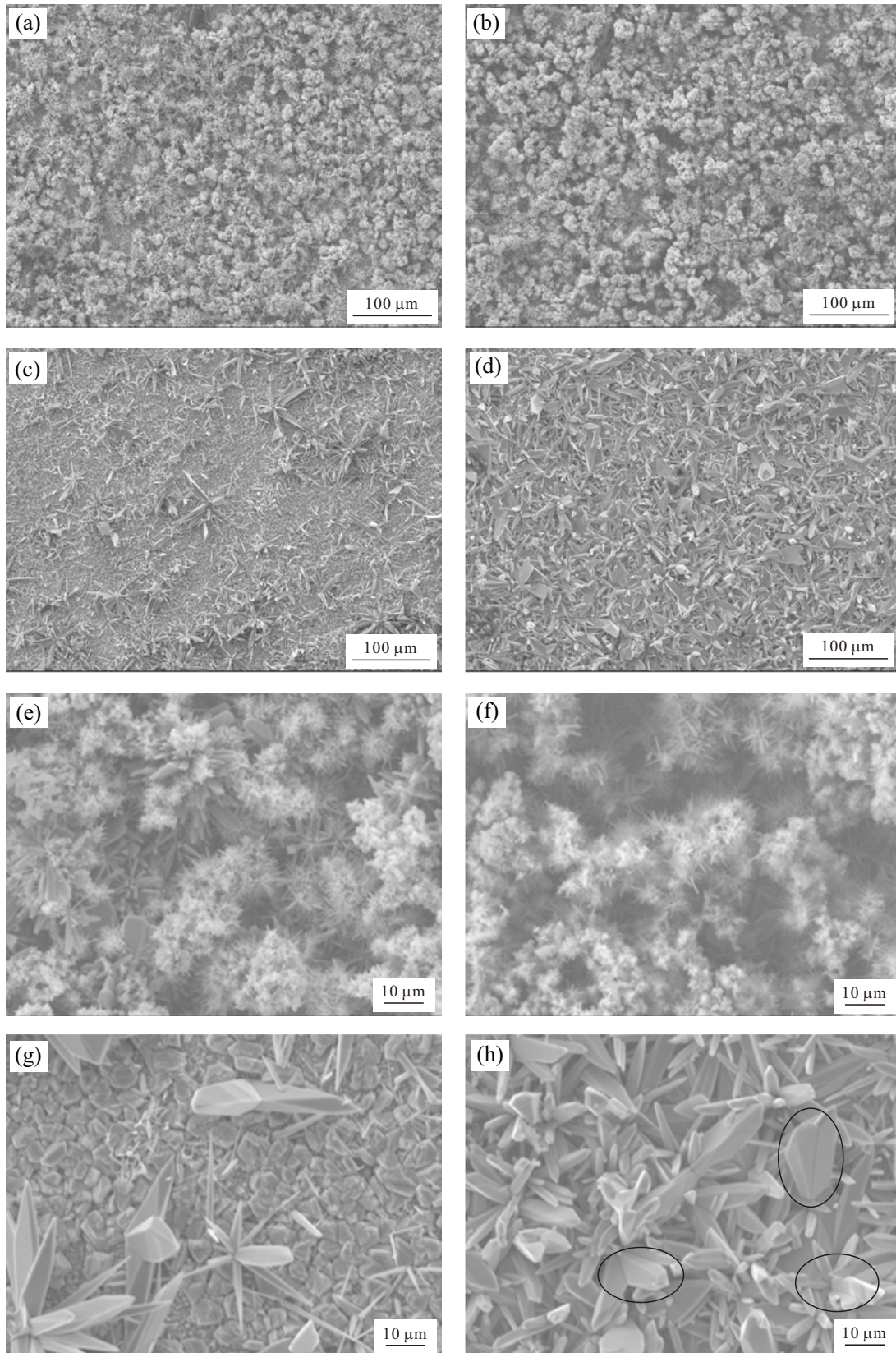
Fig.3 Corrosion morphologies of 16Mn steel in saturated H_2S/CO_2 solution with different Cl⁻ concentrations at T=80 ℃, pH=4, 6: (a) 57 ppm Cl⁻, pH=4; (b) 100 ppm Cl⁻, pH=4; (c) 57 ppm Cl⁻, pH=6; (d) 100 ppm Cl⁻, pH=6. (e)-(h) Magnified images of (a)-(d), respectively

corrosion products are composed of very small, needle-like, flocculent products, as well as blocky corro-

sion products between the globular clusters shown in Figs.3(e) and 3(f). The clustered and blocky corrosion

products present irregular arrangements, and the resultant corrosion film is generally loose. The difference in the corrosion products in Fig.3(f) from that of Fig.3(e) is the improved tightness of the corrosion film in the former because of the more uniform distribution of the needle-like, flocculent products in Fig.3(f) than in Fig.3(e). Furthermore, the blocky corrosion products almost disappear in the former case. The compactness of corrosion film gradually becomes greater with increasing Cl^- concentration at pH 4, as confirmed in Figs.3(a) and 3(b) as well as in Figs.3(e) and 3(f). A regular arrangement of the needle bar corrosion products with different sizes is found on the steel surface in Fig.3(h). The corrosion film comprises many hexagon-shaped particles with regular arrangements. Meanwhile, some triangular pyramid-like corrosion products are noticed on the surface of the corrosion film shown in Fig.3(g). The tightness of the corrosion film in this condition is the greatest among all of the samples. The grains of the corrosion products are arranged regularly at 57 ppm Cl^- in saturated H_2S/CO_2 solution at pH 6 and become irregular in Fig.3(h).

Fig.4 displays the surface morphology of the sample after removing the corrosion products from the two types of corrosive solution. Figs.4(a) and 4(b) show the surface morphology of the sample after removing the corrosion products from saturated H_2S solution at pH=4, T=80 ℃, and 57 ppm Cl^-. The corrosion pits distribute uniformly on the surface of the sample (Fig.4(a)). Many small corrosion pits are noticed between the larger corrosive pits, and the initial corrosion pit appears around such structures, as shown in Fig.4(b). Figs.4(c) and 4(d) display the surface morphology of the sample after the removal of corrosion products from saturated H_2S/CO_2 solution at pH=4, T=80 ℃, and 57 ppm Cl^-. Figs.4(c) and 4(d) indicate that the presence of CO_2 in the corrosive medium leads to the local corrosion phenomenon. The area on the corrosion surface with serious local corrosion is shown in Fig.4(c). The corrosion pits almost connect with one another (Fig.4(d)). The corrosion process is governed by the homogeneous corrosion in saturated H_2S solution containing a certain Cl^- concentration (Figs.4(a) and 4(b)). The corrosion rate of 16Mn steel in saturated H_2S solution is higher than that in saturated H_2S/CO_2 solution under the same conditions, such as pH and Cl^- concentration. The corrosion process is governed by homogenous corrosion accompanied by local corrosion in saturated H_2S/CO_2
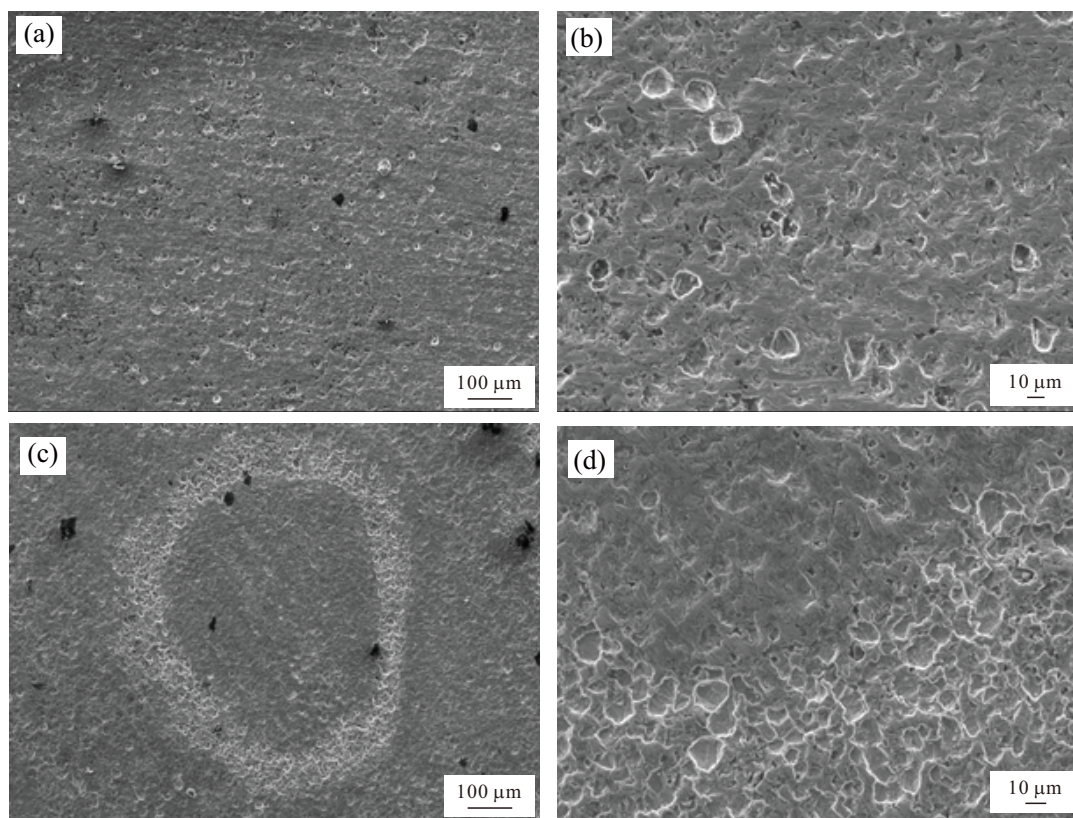

Fig.4 Corrosive morphologies after removing the corrosion products from solutions under different conditions: (a) pH=4, T=80 ℃, saturated H_2S solution with 57 ppm Cl^-; (b) magnified view of (a); (c) pH=4, T=80 ℃, saturated H_2S/CO_2 solution with 57 ppm Cl^-; and (d) magnified view of (c)

solution (Figs.4(c) and 4(d)).

3.3 Analysis of the corrosion products

Fig.5 reveals the EDS analysis results of the corrosion products of different shapes obtained under different conditions. The EDS analysis results indicate that the main elements in the corrosion products are S and Fe. Fig.5(a) displays the EDS result of the blocky corrosion products in the saturated H_2S solution lacking Cl⁻ at pH 4. The atomic ratio of Fe/S is 1/0.968, which suggests that this kind of corrosion product belongs to S-deficient iron sulfide (FeS_{1-x}). This kind of iron sulfide possesses a square crystal structure, which characterizes a metastable sulfide[22]. This kind of iron sulfide could change into iron sulfides with other structures with increasing corrosion time or elevated temperature [22]. However, the iron sulfide does not confer protection to the base metal during corrosion. Furthermore, x=0.005 7–0.064 corresponds to the atomic ratio of Fe/S at 1/0.936–0.994 3. The blocky corrosion products correspond to S-deficient iron sulfide with a square crystal structure. This characterization is achieved on the basis of the atomic ratio analysis and the corrosion morphology shown in Figs.5(a) and 2(e), respectively. On the other hand, Fig.5(b) displays the EDS result of the long, claviform corrosion products with regular arrangement in the saturated H_2S/CO_2 solution containing 100 ppm Cl⁻ at pH 6. The atomic ratio of Fe/S is 0.948/1, which indicates that this kind of corrosion product belongs to the Fe-deficient iron sulfide ($Fe_{1-x}S$). The crystal structure of $Fe_{1-x}S$ often comprises monoclinic and hexagonal crystals [22] that do not usually change once formed. Unlike the earlier example, this iron sulfide confers some protection to the base metal during corrosion. Meanwhile, x=0–0.14 corresponds to

the atomic ratio of Fe/S at 0.86-0.999/1. The compactness of the corrosion film composed of $Fe_{1-x}S$ is higher than that comprising sulfides exhibiting other crystal structures, which increases the resistance against ion transport during corrosion. The long, claviform corrosion products are noticed to correspond to the Fe-deficient iron sulfide with monoclinic or hexagonal crystal structure as revealed by the atomic ratio analysis and corrosion morphology shown in Figs.5(b) and 3(h), respectively. Fig.5(c) presents the EDS analysis results of the small, needle-like, flocculent corrosion products in the saturated H_2S/CO_2 solution containing 57 ppm Cl⁻ at pH 4. The ratio of Fe/S is 1/0.683 under this condition. The percentage content of Fe is much higher than that of S in this kind of iron sulfide, which indicates that this sulfide belongs to high-iron sulfide [23-25]. The corrosion film composed of this kind of iron sulfide is loose and easily peels off from the corroded surface. The velocity of ion transport is high under this condition, which results in the higher corrosion rate shown in Fig.1(b) and corresponds to the loose corrosion products shown in Fig.3(e).

Fig.6 shows the XRD patterns of the corrosion products in different corrosive solutions. Fig.6(a) indicates that the main phases are composed of $Fe_{(1-x)}S$ (Fe-deficient iron sulfide) accompanied with a small amount of $FeS_{(1-x)}$ for the long, claviform corrosion products in saturated H_2S/CO_2 solution containing 100 ppm Cl⁻ at pH 6[22]. Such results agree with the earlier EDS findings. The corrosion products grow and arrange regularly during the corrosion process under this condition, thereby forming a compact corrosion film. The S-deficient iron sulfide is characterized by a small amount of particle corrosion products with irregular

Element	Content/wt%	Content/at%
SK	35.62	49.193
FeK	64.38	50.807
Matrix	Correction	ZAF

(a)

Element	Content/wt%	Content/at%
SK	37.71	51.33
FeK	62.29	48.67
Matrix	Correction	ZAF

(b)

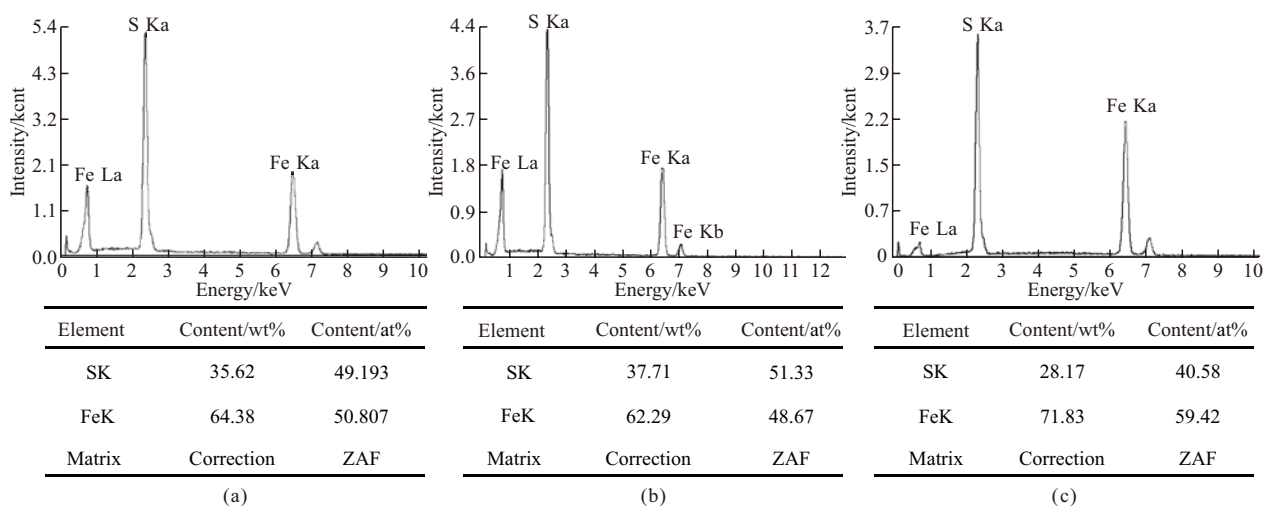| Element	Content/wt%	Content/at%
SK	28.17	40.58
FeK	71.83	59.42
Matrix	Correction	ZAF

(c)

Fig.5 EDS analysis results of corrosion products under different conditions: (a) blocky corrosion products with irregular distribution; (b) long claviform corrosion products with regular distribution; (c) the small needle-like flocculent corrosion products
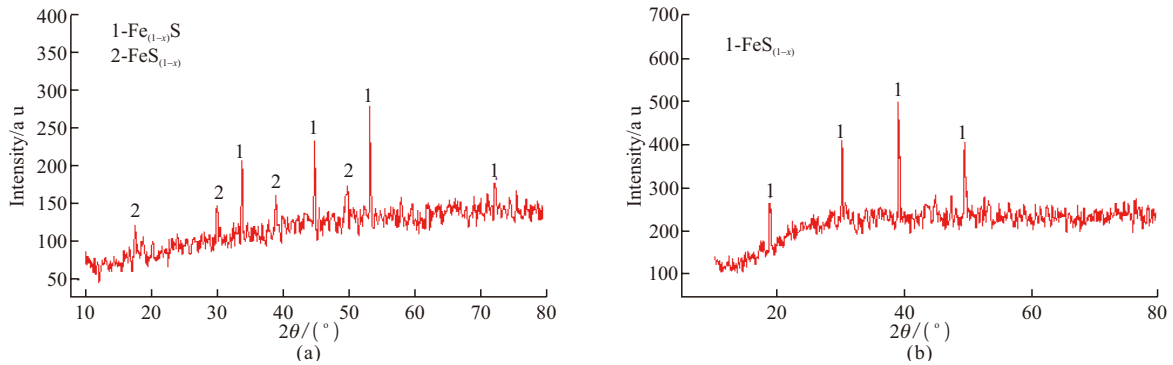
Journal of Wuhan University of Technology-Mater. Sci. Ed. www.jwutms.net Oct. 2018

1213

Fig.6 XRD patterns of corrosion products under different corrosion medium conditions at T=80 ℃ in saturated H_2S/CO_2 solution: (a) at pH=6 containing 100 ppm Cl^- and (b) at pH=4 containing 57 ppm Cl^-
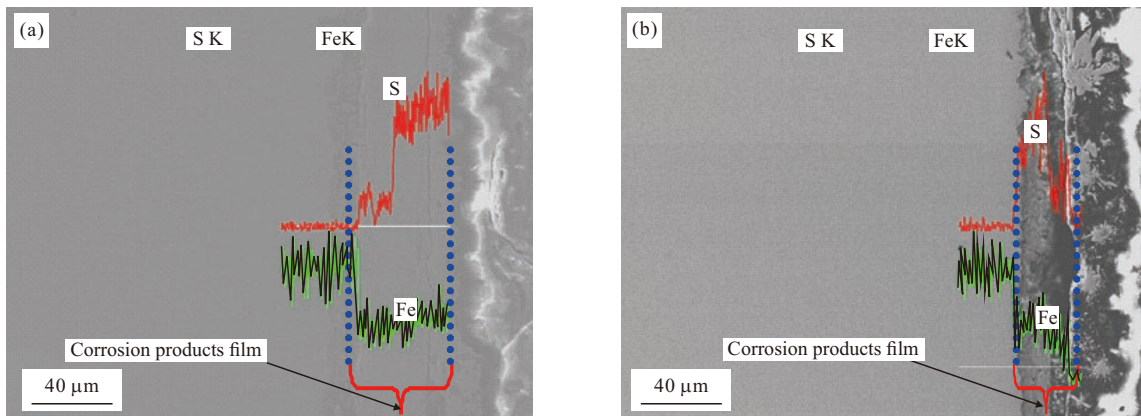

Fig.7 EDS analysis across the section from the metal substrate to the corrosion film surface under different corrosion conditions at pH=4 and T=80 ℃ in (a) saturated H_2S solution without Cl^- and (b) saturated H_2S/CO_2 solution with 57 ppm Cl^-

distribution. The main phase includes $FeS_{(1-x)}$ for the small, needle-like, flocculent corrosion products in the saturated H_2S/CO_2 solution containing 57 ppm Cl^- at pH 4 (Fig.6(b))[22]. The XRD results are consistent with the EDS results corresponding to the loose corrosion film and high corrosion rate.

Fig.7 displays the element line scan analysis results of corrosion products on the cross section of the samples under different corrosive conditions. The thickness of the corrosion film in Fig.7(b) is smaller than that in Fig.7(a), which indicates that the corrosion rate (0.465 mm/a) in saturated H_2S/CO_2 solution is lower than that in saturated H_2S solution (0.575 mm/a). The S content in the corrosion film increases from the base metal to the surface of the corrosion film in Fig.7(a). The S content at the interface between the base metal and corrosion film at a certain width is lower than that in other area. Then, the S content increases and becomes approximately constant until the surface of corrosion film is reached (Fig.7(a)). The S content increases gradually from the interface between the base metal and corrosion film to the surface of the corrosion film, and the Fe content decreases slightly within a certain range (Fig.7(b)). The corrosion products correspond to

the iron sulfides drawn from the above-mentioned EDS analysis results.

3.4 Discussion

The corrosion rate decreases with increasing Cl^- concentration in the saturated H_2S solution at pH 4. Conversely, the corrosion rate increases with increasing Cl^- concentration in the saturated H_2S solution at pH 6. The corrosion rate also decreases with increasing Cl^- concentration in the saturated H_2S/CO_2 solution at pH 4. Furthermore, the corrosion rate first increases with increasing Cl^- concentration then decreases when the Cl^- concentration exceeds 100 ppm in the saturated H_2S/CO_2 solution at pH 6. The hydrogen evolution reaction characterizes the corrosion process for 16Mn steel in saturated H_2S or H_2S/CO_2 solution at pH 4. The net content of H^+ is high in the corrosive medium at pH 4 in the saturated H_2S or H_2S/CO_2 solution. Therefore, a sufficient number of high-density H^+ ions are available at the reaction interface for the corrosion reaction. The corrosion rate of 16Mn steel depends on the adsorption efficiency for all kinds of ions in the corrosive medium that contains Cl^- and hydrolytic ion in saturated H_2S solution. A competitive adsorption exists at the reaction interface in the coexistence of multiple ions[26]. The ra-

dius and chemical activity of Cl^- are smaller and higher, respectively, than those of HS^- or S^{2-}. Therefore, Cl^- is easily adsorbed at the reaction interface, which results in a certain dilution effect for H^+ during the corrosion reaction process. The corrosion rate decreases with increasing Cl^- concentration, as shown by the dynamic perspective in Fig.1. The external and cross-sectional shapes of the corrosion products resemble square blocks with irregular arrangement in the saturated H_2S solution lacking Cl^- (Fig.2(e)). The corrosion products include the S-deficient iron sulfides known from Fig.5(a) that does not confer protection to the base metal. The shape of the corrosion products changes into a long, claviform morphology with regular distribution and some blocky or irregularly distributed particles with further increase in Cl^- concentration (Fig.2(f)). The regularly arranged long claviform corrosion products correspond to the Fe-deficient iron sulfide, as revealed by the composition analysis in Fig.5(b). The crystal structure of the Fe-deficient iron sulfide includes hexagonal and monoclinic crystal structures [22]. The corrosion film composed of Fe-deficient iron sulfide is a protective film that could prevent ion transport from the medium to the fresh base metal to a certain extent during the corrosion process. Therefore, the corrosion rate decreases because of the introduction of some protective attribute. The net content of H^+ decreases obviously in the corrosive medium at pH 6 relative to that at pH 4. Consequently, the effective ion density decreases evidently for the corrosion reactions. The bottleneck for the corrosion reactions lies on the ion transmission when the reaction thermodynamics are unchanged. The active ion Cl^- could promote the ion transmission efficiency under this condition with increasing Cl^- concentration[27]. The corrosion products form a corrosion film exhibiting some protective property, and this film is composed of long, claviform Fe-deficient iron sulfides in the corrosive medium lacking Cl^- at pH 6 (Figs.2(g) and 5(b)). With increasing Cl^- concentration, the long, claviform corrosion products partly change into blocky shapes or particles and small, needle-like, flocculent corrosion products that correspond to the S-deficient iron sulfide (Fig.2(h)). These results may confirm that increasing the Cl^- concentration in solution could promote the formation of Fe-deficient iron sulfide in acidic corrosive solution and that Cl^- promotes the formation of Fe-deficient iron sulfide in the nearly neutral solution. The corrosion rate decreases with increasing Cl^- concentration in the saturated H_2S/CO_2 solution at pH 4 because of the Cl^- dilution effect. Moreover,

the change in corrosion rate is not apparent when the Cl^- concentration exceeds 100 ppm. The corrosion products are mainly composed of small, needle-like, flocculent particles. A small amount of blocky corrosion products with irregular arrangement (Fig.3(e)) are produced when the Cl^- concentration is low. The distribution of the small, needle-like, flocculent corrosion products tends to become regular with increasing Cl^- concentration (Fig.3(f)), coupled by the slight decrease in corrosion rate. The change in corrosion rate becomes hardly noticeable when the density of the small, needle-like, flocculent corrosion products reaches a certain level. The small, needle-like, flocculent corrosion products correspond to the S-deficient iron sulfide lacking a protective attribute (Fig.6(b)). Local corrosion usually occurs when the corrosive medium contains CO_2, and the overall corrosion rate does not change markedly [28]. The local corrosion trend increases obviously, as shown by the corrosion morphology obtained after the removal of the corrosion products (Fig.4(c)). The corrosion rate increases with increasing Cl^- concentration in saturated H_2S/CO_2 solution at pH 6 because the active Cl^- promotes the ion transmission efficiency under decreased H^+ net content compared with that at pH 4. The corrosion products are mainly composed of Fe-deficient iron sulfide (Figs.3(g) and (h) and 6(a)). Hexagonal crystal phases and a small amount of monoclinic crystal phases are noticed in (Fig.3(g)). The amount of monoclinic crystal phase increases with increasing Cl^- concentration, and the density of corrosion film slightly decreases during the structural transformation from hexagonal to monoclinic. The two kinds of iron sulfides include the Fe-deficient iron sulfide that confers a protective property to the base metal (Fig.6(a)) [22]. Therefore, the corrosion rate first increases and then decreases with increasing Cl^- concentration. The corrosion process is controlled by H_2S as $P_{CO_2}/P_{H_2S} < 200$ in the coexistence of H_2S and CO_2[29,30]. No $FeCO_3$ is detected among the corrosion products in this research.

4　Conclusions

The corrosion rate of 16Mn steel decreases with increasing Cl^- concentration in the saturated H_2S or H_2S/CO_2 solution at pH 4 and 80 ℃. Conversely, the corrosion rate of the 16Mn steel increases with increasing Cl^- concentration in saturated H_2S solution at pH 6. The corrosion rate of 16Mn steel first increases and then decreases with increasing Cl^- concentration in saturated H_2S/CO_2 solution at pH 6. Meanwhile, the cor-

rosion rate does not change obviously with the addition of CO_2 into the corrosive medium, and the local corrosion trend increases. Two kinds of corrosion products are found. One is the S-deficient iron sulfide (FeS_{1-x}) with external and cross-sectional shapes resembling a square block and irregular arrangement. The corrosion film composed of FeS_{1-x} does not confer a protective attribute to the base metal. The second kind of sulfide corresponds to the Fe-deficient iron sulfide ($Fe_{1-x}S$) with a long, claviform shape resembling a hexagon and small, needle-like, flocculent particles. The density of the corrosion film composed of $Fe_{1-x}S$ is higher than that composed of FeS_{1-x}. The ability to prevent ion exchange during corrosion is stronger for the corrosion film with higher density, resulting in a lower corrosion rate.

References

[1] Saito N, Tsuchiya Y, Akai Y, *et al.* Corrosion Performance of Metals for Supercritical Water, Oxidation-utilized Organic Waste-processing Reactors[J]. *Corrosion*, 2006, 62(5): 383-394

[2] Singer M, Camacho A, Brown B, *et al.* Sour Top-of-the-Line Corrosion in the Presence of Acetic Acid[J]. *Corrosion*, 2011,67 (8): B1-B16

[3] Lashkari M, Arshadi M R. DFT Studies of Pyridine Corrosion Inhibitors in Electrical Double Layer: Solvent, Substrate and Electric Field Effects[J]. *Chem. Phys.,* 2004, 299(1): 131-137

[4] Hamzah R, Stephenson D J, Strutt J E. Erosion of Material used in Petroleum Production[J]. *Wear*, 1995, 186/ 187: 493-496

[5] Stack M M, Abdulrahman G H. Mapping Erosion-corrosion of Carbon Steel in Oil Exploration Conditions: Some New Approaches to Characterizing Mechanisms and Synergies[J]. *Tribol. Int.,* 2010, 43 (7): 1 268-1 277

[6] Chiang K T, Dunn D S, Cragnolino G A. Effect of Simulated Groundwater Chemistry on Stress Corrosion Cracking of Alloy 22[J]. *Corrosion*, 2007,63(10): 940-950

[7] Schroer C, Konys J, Novotny J, *et al.* Material Performance in Chlorinated Supercritical Water Systems[J]. *Corrosion*, 2007, 63(1): 46-62

[8] Kappes M, Frankel G S, Sridhar N, *et al.* Corrosion Behavior of Carbon Steel in Acidified, Thiosulfate- Containing Brines[J]. *Corrosion*, 2012, (68): 872-884

[9] Mendibide C, Michaud H, Pineau F, *et al.* Role of the Machining Residual Stress on the Sulfide Stress Cracking Resistance of Carbon Steel Evaluated According to NACE TM0177 Method A[J]. *Corrosion*, 2012, 68(10): 897-903

[10] Yang Y F, Scantlebury J D, Koroleva F, *et al.* Underprotection of Mild Steel in Seawater and the Role of the Calcareous Film[J]. *Corrosion*, 2012, 68 (5): 432-440

[11] Ma H Y, Cheng X L, Li G Q, *et al.* The Influence of Hydrogen Sulfide on Corrosion of Iron under Different Conditions[J]. *Corros. Sci.,* 2000, 42(10): 1 669-1 683

[12] Pessu F, Barker R, Neville A. The Influence of pH on Localized Corrosion Behavior of X65 Carbon Steel in CO_2 Saturated Brines[J]. *Corro-sion*, 2015, 71(12): 1 452-1 466

[13] Choia Y S, Nesica S, Ling S. Effects of H_2S on the CO_2 Corrosion of Carbon Steel in Acidic Solutions[J]. *Electrochim. Acta*, 2011, 56(4): 1 752-1 760

[14] W Sun. *Kinetics of Iron Carbonate and Iron Sulfide Scale Formation in CO_2/H_2S Corrosion*[D]. Ohio: Ohio University, 2006

[15] Hu Y B, Dong C F, Sun M, *et al.* Effects of Solution pH and Cl⁻ on Electrochemical Behavior of an Aermet100 Ultra-high Strength Steel in Acidic Environments[J]. *Corros. Sci.*, 2011, 53(12): 4 159-4 165

[16] Asahi H, Ueno M, Yonezawa T. Prediction of Sulfide Stress Cracking in high-strength Tubulars[J]. *Corrosion*, 1994, 50(7): 537-545

[17] Hara T, Asahi H, Ogawa H. Conditions of Hydrogen-Induced Corrosion Occurrence of X65 Grade Line Pipe Steel in Sour Environments[J]. *Corrosion*, 2004, 60(12): 1 113-1 121

[18] Tribollet B, Kittel J, Meroufel A, *et al.* Corrosion Mechanism in Aqueous Solutions Containing Dissolved H_2S. Part 2: Model of the Cathodic Reactions on a 316L Stainless Steel Rotating Disc Electrode[J]. *Electrochim. Acta*, 2014, 124(1): 46-51

[19] Linter B R, Burstein G T. Reactions of Pipeline Steels in Carbon Dioxide Solutions[J]. *Corros. Sci.,* 1999, 41(1): 117-139

[20] Teysseyre S, Was GS. Stress Corrosion Cracking of Austenitic Alloys in Supercritical Water[J]. *Corrosion*, 2006, 62(12): 1 100-1 116

[21] Beerling D J, Lake J A, Berner R A, *et al.,* Carbon Isotope Evidence Implying High O_2/CO_2 Ratios in the Permo-carboniferous Atmosphere[J]. *Geochim. Cosmochim. Ac.*, 2002, 66(21): 3 757-3 767

[22] David R, George W Luther H. Chemistry of Iron Sulfides[J]. *J. Am. Chem. Soc.,* 2007, 107(2): 514-562

[23] Sosa E, Cabrera-Sierra R, García I. The Role of Different Surface Damages in Corrosion Process in Alkaline Sour Media[J]. *Corros. Sci.*, 2002, 44(7): 1 515-1 528

[24] Yang L, Sridhar N, Pensado O, *et al.* An *in-situ* Galvanically Coupled Multielectrode Array Sensor for Localized Corrosion[J]. *Corrosion*, 2002, 58(12): 1 004-1 014

[25] Fragiel A, Serna S, Pérez R. Electrochemical Study of Two Microalloyed Pipeline Steel in H_2S Environments[J]. *Int. J. Hydrogen Energ.*, 2005, 30(12): 1 303-1 309

[26] Malo J M, Uruchurtu J, Corona O. Corrosion Detection of Mild Steel in a Two-phase Hydrocarbon/ electrolyte System under Flow Conditions using Electrochemical Noise[J]. *Corrosion*, 2002, 58(11): 932-940

[27] Colominas S, Mclafferty J, Macdonald D D. Electrochemical Studies of Sodium Borohydride in Alkaline Aqueous Solutions using a Gold Electrode[J]. *Electrochim. Acta*, 2009, 54(13): 3 575-3 579

[28] Cao L, Frankel G S, Sridhar N. Effect of Chloride on Stress Corrosion Cracking Susceptibility of Carbon Steel in Simulated Fuel Grade Ethanol[J]. *Electrochim. Acta*, 2013, 104(1): 255-266

[29] Yin Z F, Liu L, Zhang Y Q. Corrosion Behavior of SM 80SS Tube Steel in Stimulant Solution Containing H_2S and CO_2[J]. *Electrochim. Acta*, 2008, 53(10): 3 690-3 700

[30] Ramanarayanan T A, Chun C M. Metal Dusting Corrosion of Metals and Alloys[M]. *Developments in High Temperature Corrosion and Protection of Materials*. Princeton: Woodhead Publishing, 2008